Development of a calcium sulfoaluminate-Portland cement binary system for twin-pipe 3D concrete printing

Yaxin Tao[1], Manu K. Mohan[1], A.V. Rahul[2], Geert De Schutter[1], Kim Van Tittelboom[1]

[1]Magnel-Vandepitte Laboratory for Structural Engineering and Building Materials, Ghent University, Ghent, Belgium

[2]Department of Civil Engineering and Environmental Engineering, Indian Institute of Technology Tirupati, Tirupati, India

Abstract

Recently, the twin-pipe pumping (TPP) system has been developed for 3D concrete printing which involves pumping two mixtures, typically a Portland cement-based mixture and a pure limestone powder-based mixture that contains an accelerator. Following this, the two mixtures are allowed to be intermixed in a static mixer placed just prior to the nozzle which causes immediate stiffening and a very high buildability for the printed concrete post-extrusion. However, the flow division pattern produced by the mixing baffles of the static mixer results in striations consisting of unmixed limestone powder resulting in weak zones that lower the mechanical strength of the printed element. In this study, we present a TPP system consisting of Portland cement-based mixtures and a borated calcium sulfoaluminate (CSA) cement-based mixture. The mixtures are capable of reacting independently with water as compared to the pure limestone powder-based mixture. After getting blended in the static mixer right before extrusion, the retardation in the borated CSA cement is destroyed by the alkaline component contained in the other stream, leading to the rapid hardening and a high construction rate post extrusion from the nozzle. The hydration characteristics were studied using a Vicat penetrometer, isothermal calorimetry, and ultrasonic pulse velocimetry, while the early age mechanical behavior was characterized by using uniaxial unconfined compression and slow penetration tests. Results indicate that Portland cement alone cannot produce enough alkalinity to destroy the ulexite phase and reinitiate the hydration of CSA cement, while adding a nominal dosage of calcium hydroxide can provide enough increase in pH to design a system suitable for the stiffening control. However, abundant calcium hydroxide would reduce the hydration rate at later ages due to the dilution effect, as indicated by the P-wave velocity evolution and yield stress evolution. In addition, the hardened behavior of printed elements was studied by

performing compression and flexural tests. Results show that the CSA-Portland cement binary binder system avoids the formation of weak zones and hence improves the mechanical behavior.

Keywords: Twin-pipe pumping, 3D concrete printing, stiffening control, Portland cement, CSA cement, static mixer.

1 Introduction

3D concrete printing (3DCP) technology is revolutionizing the construction industry with many merits over traditional construction methods, such as higher design freedom, raised construction efficiency, less material consumption, reduced labor force, and improved worker safety [1, 2]. For example, a recent report showed that 3DCP technology has the potential to increase the construction speed by 50-80% with reducing material consumption by 30-60% [3]. Different types of methods have been proposed including extrusion-based printing, powder-bed printing, and shotcrete-based printing [4-6]. Among them, extrusion-based printing has gained the most attention. The process of extrusion-based 3DCP includes (1) pumping the fresh material through a pipeline, (2) extruding the material from a nozzle, and (3) depositing the material layer-by-layer to form the structure.

High fluidity and low structural build-up of the material is expected for an effective and continuous pumping process without any blockage, while the material should gain enough strength and possess high structural build-up to avoid any collapse or buckling failure after extrusion. Two potential strategies can be used: enhancing the thixotropic characteristic or introducing an intervention to speed up the structural build-up of the fresh material during extrusion [7]. Introducing thixotropic additives such as nanoclay or nanosilica in the initial mixture is an option, which would facilitate the structural build-up of the fresh material at rest [8-10]. Merely relying on the thixotropic properties of fresh concrete does not allow the structure to be built very high as the yield stress development is still limited without any acceleration of the cement hydration [11]. Furthermore, a high addition level of thixotropic agents would drastically reduce the fluidity of the fresh material, resulting in high pumping pressure or even pipe blockage.

Another strategy for achieving high buildability is introducing an intervention that causes the transition of the fresh material from a visco-elastic/visco-plastic state to a pseudo-solid state shortly

after extrusion. A series of intervention strategies have been proposed including chemical, thermal, magnetic, and ultra-sonic manners [12-15]. Among them, chemical intervention is the most effective way [16]. To this end, an accelerator is normally used as a chemical trigger for extrusion-based 3D concrete printing because of its commercial availability [17]. Several approaches have been proposed such as encapsulation and inline mixing. For the former, the accelerator can be stored in an encapsulated form with the initial mixture followed by activating at the print head, i.e. heating above the melting temperature of the shell material to dissolve the capsules [3]. Unfortunately, the accelerator is not uniformed distributed due to the floating tendency and segregation of coarse capsules. At this stage, injecting liquid accelerator into the fresh material is the most practical solution and this approach has already been successfully used in several applications such as shotcrete and two-fluid grouting [18, 19]. Different from the shotcrete technology with a pneumatic actuator, extrusion-based 3D concrete printing requires a much lower extrusion velocity and a continuous filament. The homogenous dispersion of accelerator in the fresh material remains a big challenge. Different types of inline mixing systems have been designed to solve this issue in 3DCP and most of them use the approach of injecting liquid accelerator and stirring the mixture by using a dynamic mixer [16, 20, 21]. The mixing efficiency of the dynamic mixer strongly depends on the blade design. Further, dead zones may form due to the high-velocity gradient inside the dynamic mixer. Another weakness is the difficulty to maintain the complicated components [15].

Alternatively, a twin-pipe pumping (TPP) system has been developed by using a limestone powder suspension as the carrier material for the chemical trigger (such as an accelerator) and a motionless static mixer for the inline mixing purpose [22]. This system was primarily designed for Portland cement, where two constituent mixtures including a Portland cement-based mixture (without accelerator) and a limestone powder-based mixture (without cement but with a high dosage of shotcrete accelerator) are pumped separately and blended via a motionless static mixer right before extrusion. Both constituent mixtures are designed to have an initial long open time, and after being combined, the accelerator contained in the limestone powder-based mixture would soon interact with the Portland cement present in the other mixture, leading to a very high structural build-up rate after extrusion. Recent studies have shown that the mechanical integrity of printed elements can be quite low due to the formation of striations originating from the flow division pattern, especially when a limited number of mixing elements are used in the static mixer [23]. Since

limestone powder as such cannot react with water, the limestone powder-based striations are the weak zones which reduce the overall mechanical strength of the 3D printed element (see Fig. 1) [23, 24].

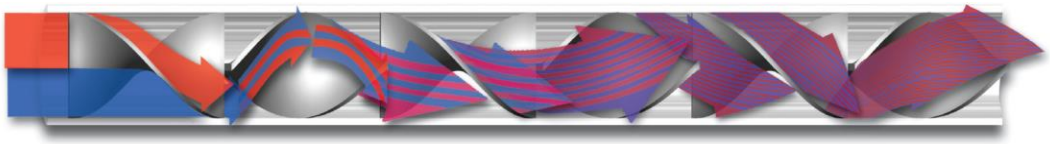

(a)

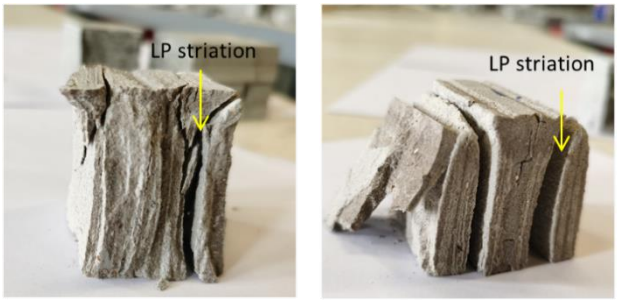

(b)

Fig. 1 (a) Flow divisions in a static mixer that result in the formation of striations in the printed element and (b) failure planes that pass through the weak limestone-based striations during the compression testing of printed elements, adapted from [23, 24].

In this study, we present the development of a calcium sulfoaluminate (CSA)-Portland cement binary system designed for the TPP application. CSA cement is a kind of hydraulic binder containing high amounts of ye'elimite. It has several benefits such as low carbon emissions and promising fast hardening properties [25]. Compared to the limestone-based system, both the CSA and Portland cement can react independently with water, thus eliminating the formation of weak zones and improve the mechanical integrity in the 3D printed structure. We present early-age hydration and rheological studies that demonstrate the high open time and workability of the CSA and Portland cement-based mixture when used separately without intermixing. It should be noted that the CSA cement-based mixture is retarded to avoid fast setting. However, upon intermixing the two fluids, the alkalinity in the Portland cement-based mixture destroys the retarding effect of borax in the CSA cement-based mixture, leading to the rapid stiffening for high buildabilty. The rapid stiffening that occurs in the combined mixture is studied by performing Vicat tests, uniaxial

compression tests, slow penetration tests, and ultrasonic pulse velocimetry measurements. The mechanical behavior of the combined mixture in the hardened state is investigated by using cubic and prismatic specimens extracted from 3D printed wall elements.

2 Experimental program

2.1 Materials and sample preparation

Two types of binders were used in this study including Portland cement (CEM I 52.5N by Holcim, Belgium) and calcium sulfoaluminate (CSA) cement (i.tech ALI CEM GREEN® by Italcementi, Italy). The specific gravity is 3.16 and 3.15, respectively. The chemical composition and minerological compostion of both cements is shown in Table 1 and Table 2, respectively.

Table 1 Chemical composition and loss on ignition of Portland cement and CSA cement (%).

Cement	CaO	SiO_2	Al_2O_3	Fe_2O_3	MgO	Na_2O	K_2O	SO_3	Cl^-	LOI
Portland cement	64.3	18.3	5.2	4.0	1.4	0.32	0.43	3.5	0.06	2.7
CSA cement	41.5	8.14	23.2	1.05	3.22	0.86	0	18.36	0	1.45

Table 2 Minerological compostion of Portland cement and CSA cement (%).

Cement	Portland cement	CSA cement
Ye'elimite	-	54.64
Anhydrite	-	23.7
Basanite	-	0.30
Periclase	-	2.4
C_3S	66.41	-
C_2S	9.04	18.97
C_3A	6.4	-
C_4AF	9.26	-
Calcite	5.17	-
Quartz	0.63	-
Gypsum	2.63	-

Silica sand with a maximum particle size of 2 mm and a specific gravity of 2.65 was used for both constituent mixtures (CSA cement-based and Portland cement-based). Borax, i.e. disodium tetraborate decahydrate ($Na_2B_4O_7 \cdot 10H_2O$), was used as retarder for CSA cement, aiming at achieving sufficient open time for the CSA cement-based mixture. To further increase the alkalinity of the Portland cement-based mixture, calcium hydroxide (CH) was used as an additive. The increase in pH reinitiates the hydration of the CSA cement-based mixture which was retarded by using borax. The specific gravity of calcium hydroxide was 2.24. The particle size distributions of sand, CSA cement, Portland cement, and calcium hydroxide are shown in Fig. 2. In addition, a liquid superplasticizer with a solid concentration of 35% (BASF, Master Glenium 51, Germany) was used in the Portland cement-based mixture.

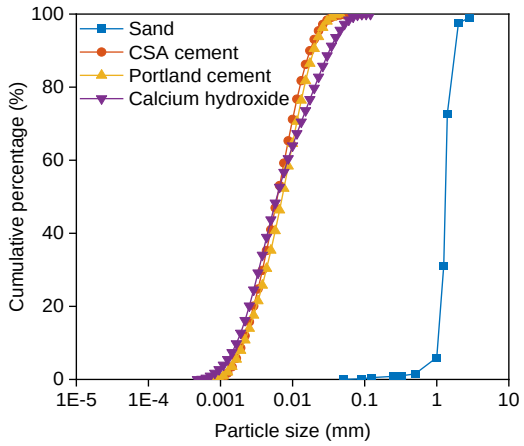

Fig. 2 Cumulative percentage of sand, CSA cement, Portland cement, and calcium hydroxide.

The mixture design of the CSA cement-based mixture (mixture A) and of four Portland cement-based mixtures (mixture B0, B2, B4, and B6) is shown in Table 3. The substitution rate of calcium hydroxide was 0%, 2%, 4%, and 6% by the weight of Portland cement for the mixtures B0, B2, B4, and B6, respectively. The dosage of borax in the mixture A was 2% by the weight of CSA cement and the dosage of superplasticizer was 0.6% by the weight of Portland cement for the mixtures B. The dosages of borax, superplasticizer, and calcium hydroxide were determined based on previous studies [26]. The sand to cement ratio was 1.2 and the water to cement ratio was 0.35 for all constituent mixtures (CSA cement for the mixture A and Portland cement for the mixture B) [23, 27].

Table 3 Mixture design of mixture A and mixtures B (kg/m^3)

Mixture	Sand	CSA cement	Portland cement	Water	Borax	CH	Superplasticizer
A	1071.2	892.7	0	312.4	17.8	0	0
B0	1072.1	0	893.5	312.7	0	0	5.36
B2	1069.7	0	873.6	312.0	0	17.8	5.24
B4	1067.2	0	853.7	311.2	0	35.6	5.12
B6	1064.7	0	834.1	310.5	0	53.2	5.00

The volume ratio between the mixture A and mixture B was kept constant as 1. The combined mixture was designated as mixture, A-B0, A-B2, A-B4, and A-B6, as shown in Table 4.

Table 4 Mixture design of combined mixtures (kg/m^3).

Mixture	Sand	CSA cement	Portland cement	Water	Borax	CH	Superplasticizer
A-B0	1071.6	446.6	446.6	312.5	8.91	0	2.68
A-B2	1070.4	446.1	437.1	312.2	8.90	8.90	2.68
A-B4	1069.2	445.5	427.7	311.8	8.89	17.84	2.67
A-B6	1067.9	445.0	418.3	311.4	8.88	26.70	2.67

Paste, which had the same composition as the mixtures except for the sand listed in Table 3 and Table 4, was used for the isothermal calorimetry tests and setting time measurements. A Hobart planetary mixer was used for preparing the samples according to the following mixing procedure: (1) dry mixing all powdery materials at 140 rpm for 30 s, (2) adding water and superplasticizer (premixed in water if any) to the dry mixture and continue mixing at 140 rpm for 60 s, (3) continue mixing at 285 rpm for 30 s, (4) scraping and resting for 90 s, (5) mixing at 285 rpm for 60 s. The whole mixing procedure lasted around 270 s.

For the flow curve experiments, ultrasonic pulse velocimetry measurements, uniaxial unconfined compression tests, slow penetration tests, and mechanical tests (mold cast), the mixture was not processed by an inline mixer, but by a Hobart mixer in order to get a quasi-homogenous distribution in the mixtures, according to the following procedure: (1) dry mixing CSA cement, silica sand, and borax for the mixture A (Portland cement, silica sand, and calcium hydroxide powder for the

mixture B) at 140 rpm for 30 s, (2) adding water and superplasticizer (premixed in water if any) to the dry mixture and continue mixing at 140 rpm for 60 s, (3) continue mixing at 285 rpm for 30 s, (4) scraping and resting for 90 s, (5) mixing at 285 rpm for 60 s. The whole mixing procedure lasted around 270 s for both mixtures. Immediately, the two constituent mixtures were blended at 285 rpm for 15 s.

For the mechanical tests of 3D printed specimens, the mixtures A and B (around 30 liters) were prepared by using a pan mixer with a capacity of 50 liters. The mixing procedure is shown as follows: (1) dry mixing CSA cement, silica sand, and borax for the mixture A (Portland cement, silica sand, and calcium hydroxide powder for the mixture B) at 60 rpm for 30 s, (2) adding water and superplasticizer (premixed in water if any) to the dry mixture and continue mixing at 60 rpm for 120 s, (3) scraping and resting for 90 s, (4) mixing at 60 rpm for 180 s. The whole mixing procedure lasted around 420 s for both mixtures. Wall elements with 18 layers (layer thickness 10 mm) were produced by using the twin-pipe pumping system [22]. The length, height, and width of the wall elements were 1000 mm, 180 mm, and 50 mm, respectively. A plastic nozzle with a rectangular outlet (width 50 mm) was used. The distance of the nozzle to the basement equals to the thickness of one printed layer (10 mm). The mixtures A and B were delivered separately by using two pumps (Rudolf STROBOT 407) and blended via a static mixer with 18 mixing baffles. The volume flow was set identically for both pumps. The geometrical parameters of the static mixer can be found in previous work of the authors [28]. The printing speed was 200 mm/s. The printed wall elements were first kept in an ambient environment for 24 hours. Afterwards, prismatic specimens (160×40×40 mm^3) and cubic specimens (40×40×40 mm^3) were cut from the wall elements and cured in a controlled environment (temperature 20 °C, relative humidity 95%) until the age of 7 days. The details about the cutting positions are shown in Fig. 4 [22].

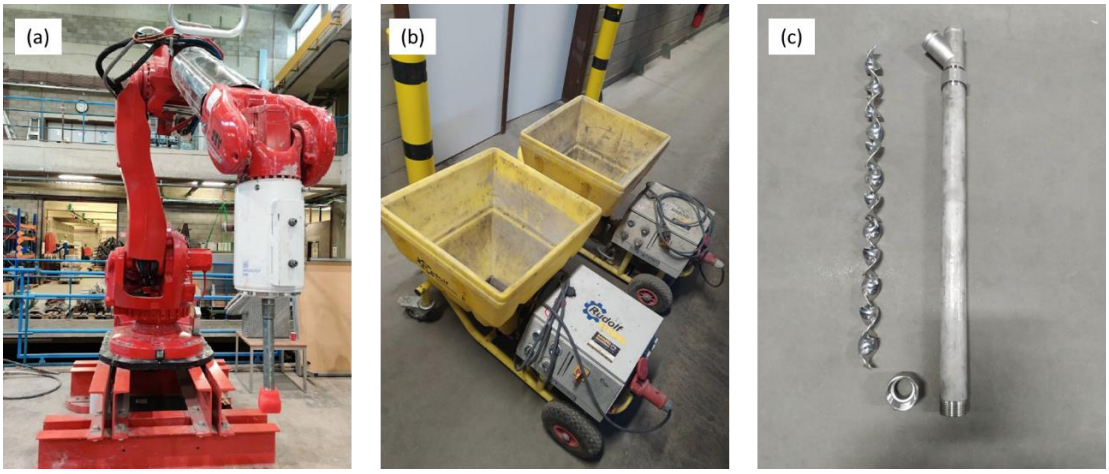

Fig. 3 Twin-pipe pumping system: (a) robotic arm, (b) pumps, and (c) static mixer.

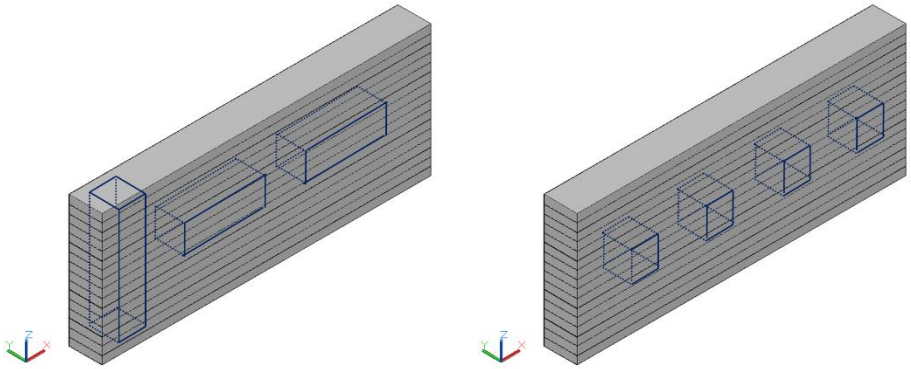

Fig. 4 Extracting specimens from the wall element to test the mechanical behavior including (a) flexural strength and (b) compressive strength, adapted from [22].

2.2 Testing procedures

2.2.1 Flow curve experiments

A stress-controlled rheometer (MCR 52, Anton Paar) was used for flow curve measurements of both the CSA cement-based mixture and the Portland cement-based mixtures. A building materials cell (inner diameter 70 mm, depth 99 mm) with vertical corrugations (width 1 mm) was used together with a 4-blade vane rotor (blade width 40 mm, blade height 15 mm). The testing procedure is shown in Fig. 5. Firstly, around 500 g sample was pre-sheared at a constant rotational speed of 100 rpm for 60 s and left to rest for 30 s. Afterwards, a stepwise increase and decrease of rotational

velocity (step range 20 rpm, step duration 20 s) was applied. As a follow-up, shear rates were derived from rotational speeds after applying a plug flow correction [29, 30]. The test was repeated twice for each mixture.

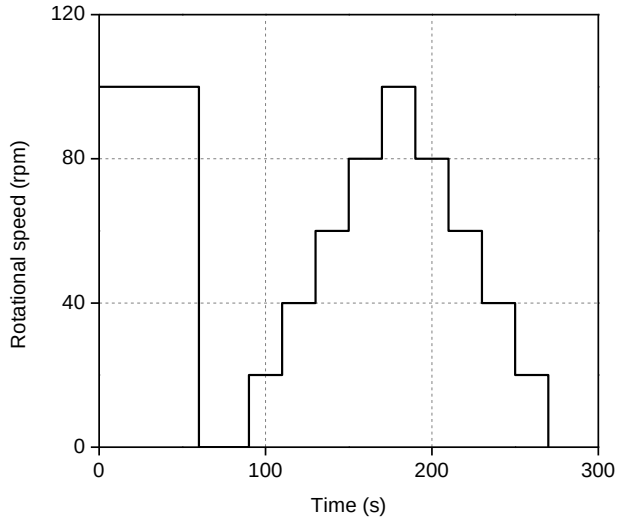

Fig. 5 Testing protocol for flow curve.

2.2.2 Setting time measurements

An automatic Vicat apparatus (Impact Test Equipment Ltd) was used to measure the initial and final setting times of the mixtures according to the standard EN 196-3:2005 [31]. A plastic mold with a depth of 40 mm and an internal diameter of 75 mm was used to contain the paste samples. The measurements were started immediately after placing the paste samples in the plastic mold. Due to a huge difference between the setting time of each mixture, different time gaps were used. The whole testing process was performed in a controlled environment (temperature 20 ℃, relative humidity 65%). The initial setting time was determined by the elapsed time from adding water to dry materials to the time when the penetration depth equaled 34 to 37 mm. The final setting time was determined by the time when the penetration depth into the sample was 0.5 mm. For combined mixtures, the measurements were carried out 3 minutes after intermixing two constituent mixtures. The test was repeated twice for each mixture.

2.2.3 Ultrasonic pulse velocimetry measurements

A FreshCon apparatus (SmartMote) was used for the ultrasonic pulse velocimetry (UPV) measurements of the mixtures [32]. The sample was loaded in a U-shaped foam rubber holder immediately after mixing and a tight transparent plastic sheet was used to cover the sample to avoid evaporation. A piezoelectric broadband transmitter was used to send ultrasonic pulse signals (20–300 kHz) which were collected every minute by using a receiver at the other end of the sample. Based on the time taken for the longitudinal wave to transmit from one end of the sample to the other, the longitudinal velocity (also called the P-wave velocity) of the sample was measured. For combined mixtures, the measurements were started 3 minutes after intermixing two constituent mixtures. The test was repeated twice for each series. More details about the experimental setup and methodology can be found in references [33, 34].

2.2.4 Isothermal calorimetry tests

A commercial conduction calorimeter (Thermometric TAM Air) was used to monitor the rate of heat evolution and cumulative heat release following NBN EN196-9 [35]. 14 g paste was prepared in a controlled environment with a constant temperature of 20 ℃ and loaded in the ampoule immediately after the mixing process. It is assumed that the temperature can be equalized in a short period after loading the sample. The measurement was performed for 24 hours for each mixture at a constant temperature of 20 ℃. For combined mixtures, the data collection was started 3 minutes after intermixing two constituent mixtures. The test was repeated twice for each mixture.

2.2.5 Uniaxial unconfined compression tests

Uniaxial unconfined compression tests (UUCT) were performed to evaluate the mechanical behavior at the early stage. The tests were performed using cylindrical specimens (diameter 70 mm and height 140 mm) at the age of 5 minutes after the combination of two mixtures [27]. A universal testing machine (Water + Bai DB) equipped with a loading cell of 250 kN was used [36]. The following testing procedure was adopted: (1) casting the fresh material in two batches (half volume for each batch) in the cylindrical mold, (2) compacting the material by 25 blows using a tamping rod (diameter 10 mm) for each time, (3) demolding the sample after 3 minutes and placing the sample at the loading position, and (4) testing the sample with a loading rate of 30 mm/min. Afterwards, the force-displacement data was used to derive the stress-strain curves based on the

geometry of the unloaded sample. The strain equals the value of vertical deformation divided by the original height of the sample. The maximum stress was taken as the unconfined compressive strength and the slope of the stress-strain graph at a strain level of 5% (within the linear elastic region) was taken as the elastic modulus [26]. The test was repeated twice for each series.

2.2.6 Slow penetration tests

The yield stress evolution was recorded by using the slow penetration test. A universal testing machine (Water + Bai DB) equipped with a loading cell of 3 kN was used. A steel shaft with a spherical front-end (diameter of 15 mm) was used [37]. After combining the mixtures A and B, the combined sample was cast in a cubic container (size of 100 mm). The measurement started when the steel sphere half emerged in the sample. A loading rate of 0.5 mm/min was used and the maximum displacement was set as 25 mm. The yield stress evolution could be derived from the force evolution [38], as shown below:

$$F = 3\pi R^2 \tau_0 \tag{1}$$

where τ_0 is the yield stress of the material (Pa), F is the measured penetration force (N), and R is the diameter of the spherical front-end (m).

2.2.7 Mechanical tests

The flexural strength at the age of 7 days was measured by using the three-point bending flexural test, following the standard NEN-EN 12390-5 [39]. The prismatic specimens were placed on two supporting rollers with a span of 100 mm and the strength was calculated according to the following equation:

$$\sigma_f = \frac{3F_f L}{2bd^2} \tag{2}$$

where σ_f is the flexural strength (MPa), F_f is the load at the middle position of the prism specimen (N), L is the supporting span (mm), b is the width of the prismatic specimen (40 mm), and d is the height of the prismatic specimen (40 mm). The test was repeated 3 times for each series. It should be noted that the flexural test of 3D printed specimens was performed in three mutually perpendicular orientations F1, F2, and F3, as shown in Fig. 6.

The compressive strength at the age of 7 days was measured by using cubic specimens, following the standard NEN-EN 12390-3 [40]. The compressive strength was calculated according to the following equation:

$$f_c = \frac{F}{A_c} \tag{3}$$

where f_c is the compressive strength (MPa), F is the maximum load at failure (N), and A_c is the cross-sectional area of the specimen on which the compressive force acts (1600 mm^2). The test was repeated 6 times for each series. For 3D printed specimens, the compression test was performed in three mutually perpendicular orientations C1, C2, and C3, as shown in Fig. 6.

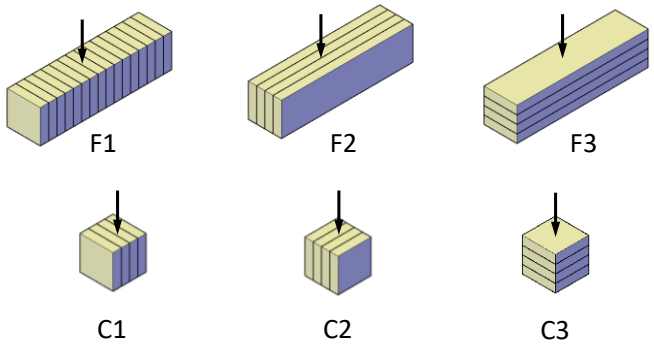

Fig. 6 Loading orientations in flexural and compression tests.

3 Results and discussion

3.1 Rheological behavior and setting of the constituent mixtures

The flow curves of the CSA cement-based mixture (mixture A) and the Portland cement-based mixtures (mixtures B) are shown in Fig. 7 and rheological parameters including yield stress and plastic viscosity are tabulated in Table 5. It can be observed that the plastic viscosity of the mixture A (1.95 Pa·s) was significantly higher than that of the mixtures B, especially the mixture B0 without the addition of calcium hydroxide (1.09 Pa·s). The lower viscosity in the mixtures B can be mainly due to the addition of superplasticizer while the mixture A contains no superplasticizer [41, 42]. Furthermore, the higher viscosity of the mixture A could be due to the higher surface interaction in CSA cement as compared to Portland cement. It was reported that the repulsive electrical force between CSA cement particles is lower, making the attraction between charged particles easier and

the attractive force stronger [43]. The other reason could be the precipitation of poorly crystallized calcium borate when adding borax to the CSA cement-based mixture. The formation of this phase can also increase the plastic viscosity of the mixture [44]. The increase in calcium hydroxide content in the mixture B enhanced the yield stress gradually. This can be attributed to the increase in solid volume fraction as the calcium hydroxide content increased [45, 46].

As reported in other studies, the yield stress and viscosity of conventional 3D printable mixtures are in the range of 600-2000 Pa and 15-40 Pa·s [26]. With regard to the twin-pipe pumping technology, both the mixtures A and B exhibited significantly lower yield stress and plastic viscosity when compared to the values of other conventional 3D printable mixtures. This is beneficial to ease the pumping operation and reduce abrasion of the pump.

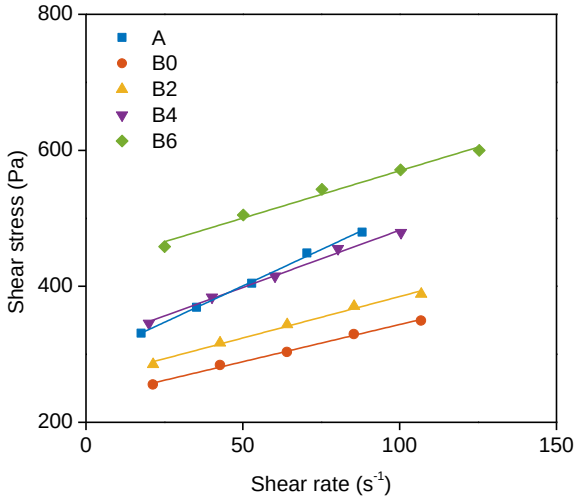

Fig. 7 Flow curve of constituent mixtures A and B (points in the graph represent mean values, n = 2, and the line represents the Bingham fit).

Table 5 Yield stress and viscosity of constituent mixtures A and B.

Mixture	Yield stress (Pa)	Viscosity (Pa·s)
A	297.1±13.4	1.95±0.07
B0	234.5±9.7	1.09±0.12
B2	263.0±17.5	1.22±0.13
B4	314.3±6.9	1.68±0.18
B6	430.7±25.6	1.39±0.24

The initial and final setting times of the constituent mixtures are listed in Table 6. The constituent mixtures A and B showed long open times, which were higher as compared to the values reported in literature [47, 48]. The retardation of the mixture A was due to the precipitation of ulexite with the addition of borax in the system [49]. The ulexite phase further covers the cement grains and inhibited the ion dissolution of anhydrous cement phases, leading to a prolonged setting time [50]. Among the different B mixtures, the setting time was the highest for the mixture B0. With the increase in calcium hydroxide content, there was a decrease observed in the setting time. This can be attributed to the increase in pH which causes an increase in the rate of hydration reaction and subsequent decrease in the induction period [51, 52]. This can also be reflected by the higher P-wave velocity of the mixtures B2, B4, and B6, as compared to that of the mixture B0 (see Fig. 8). For example, the P-wave velocity of the mixture B6 at the age of 60 min reached 439 m/s, while the value of the mixture B0 at the same age was merely 265 m/s. In addition, it can be seen that the P-wave velocity of the mixture A was higher as compared to that of the mixtures B, which can be due to the higher particle interaction in CSA cement as compared to Portland cement [43].

Table 6 Initial and final setting times of constituent mixtures A and B.

Mixture	Initial setting time (min)	Final setting time (min)
A	220.5±29.0	1260.0±56.6
B0	285.0±14.1	502.5±24.7
B2	305.0±21.2	493.4±23.5
B4	213.2±61.1	382.5±10.6
B6	239.5±7.8	412.8±25.2

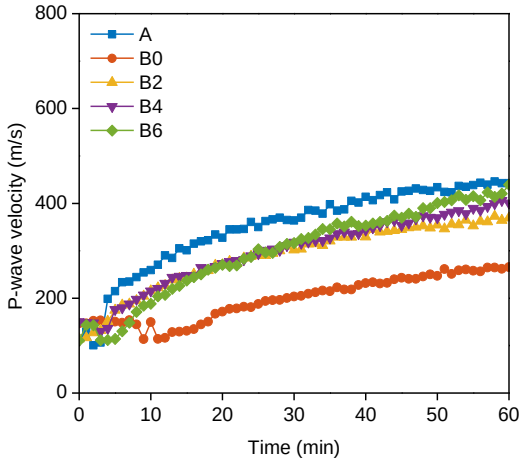

Fig. 8 Evolution of P-wave velocity of constituent mixtures A and B.

3.2 Rapid stiffening of the combined mixture

3.2.1 Early age hydration

Fig. 9 shows the evolution of P-wave velocity for the different combined mixtures obtained from the ultrasonic pulse velocimetry (UPV) measurements. All the mixtures showed a remarkably higher P-wave velocity (over 1000 m/s at around 10 min from the onset of casting) as compared to that of the two constituent mixtures (see Fig. 8). In addition, the P-wave velocity of the combined mixtures was much higher than that of the conventional 3D printed concrete, which is in the range of 50-100 m/s [36, 44]. This indicates an increase in solid volume fraction as a result of the rapid hydration reaction. Due to the fast precipitation of hydration products for the combined mixtures, a complete path of connected particles for the P-wave transmission is formed in a short period [53].

Similar to the trends, a very high rate of heat evolution and total cumulative heat can be observed for the combined mixture obtained from the isothermal calorimetry measurements (see Fig. 10 (a) and (b)).

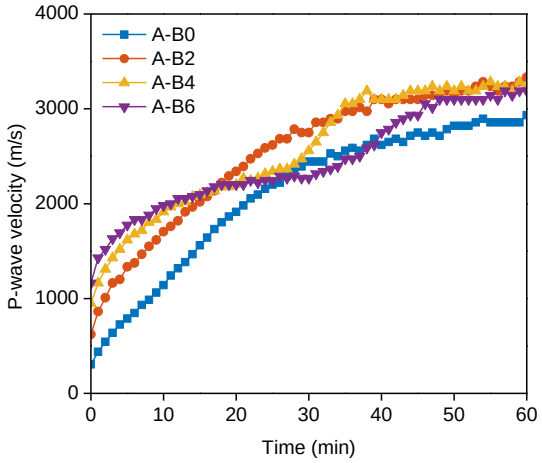

Fig. 9 Evolution of P-wave velocity of the combined mixtures.

Initially, the pH of the CSA-based mixture got lowered due to the addition of borax, used as the retarding agent. Furthermore, borax resulted in the formation of the poorly crystalline phase, ulexite which covered the surface of the CSA grains. When the CSA-based mixture was intermixed with Portland cement, the high alkalinity of the Portland cement-based mixture led to an overall increase in pH. Previous studies have shown that the increase in pH of the system will destabilize the ulexite phase [26]. Once the inhibition effect of ulexite covering the surface of ye'elimite is deminished, the ye'elimite phase presented in the CSA cement would rapidly react with sulphates (anhydrite or gypsum) to form ettrinigite and aluminium hydroxide [50]:

$$C_4A_3\bar{S} + 2C\bar{S}H_2 + 34H \rightarrow C_6A\bar{S}_3H_{32} + 2AH_3 \quad (4)$$

In addition, with the presence of calcium hydroxide and sufficient sulphates, aluminium hydroxide can further react with both to generate additional ettringite [25]:

$$AH_3 + 3CH + 3C\bar{S}H_2 + 20H \rightarrow C_6A\bar{S}_3H_{32} \quad (5)$$

Another important aspect to be discussed is the effect of calcium hydroxide on the hydration behavior of the combined mixture. In Fig. 9, the evolution of the mixture A-B0 without calcium hydroxide is much lower compared to that of the other mixtures (A-B2, A-B4, and A-B6). A similar

trend can also be observed in the cumulative heat evolution (see Fig. 10 (b)) and the setting times of the combined mixtures (see Table 7). This indicated that Portland cement alone does not result in enough alkalinity for the combined system for a very fast re-initiation of the hydration reaction required for the TPP application. Adding a small dosage of calcium hydroxide (2-6 %) resulted in a higher alkalinity and a much faster rate of hydration reaction for the combined mixture. Furthermore, in the presence of abundant calcium hydroxide in the system, the following reaction is favored to occur [54]:

$$C_4A_3\bar{S} + 8C\bar{S}H_2 + 6CH + 74H \rightarrow 3C_6A\bar{S}_3H_{32} \quad (6)$$

Compared to the reaction shown in equation (4), the above reaction produces three times the amount of ettringite for the same amount of ye'elimite being consumed [55, 56]. This leads to a higher heat evolution as seen in Fig. 10 (a) as well as faster growth in the network of a solid skeleton thus increasing the P-wave velocity in the UPV measurements (see Fig. 9).

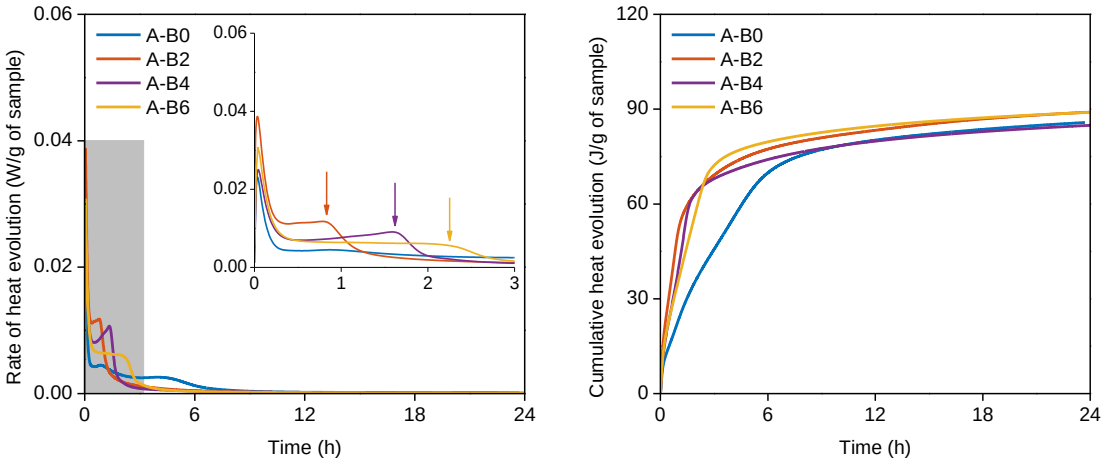

Fig. 10 (a) Rate of heat evolution and (b) cumulative heat evolution of combined mixtures.

Table 7 Initial and final setting times of the combined mixture.

Mixture	Initial setting time (min)	Final setting time (min)
A-B0	17.0±2.1	22.8±3.9
A-B2	11.8±3.2	24.0±4.2
A-B4	4.8±0.4	15.5±0.7
A-B6	3.6±0.8	13.2±4.5

3.2.2 Mechanical behavior at fresh stage

The stress versus strain curves measured in the uniaxial unconfined compression tests (UUCT) at the very early age of 5 min are shown in Fig. 11 (a). For every specimen, the stress initially increased approximately linearly as the vertical strain grew. After reaching the yielding point, the stress decreased, instead of reaching a certain plateau. This indicated a shear plane failure related to the brittleness of the specimen for the combined mixtures [57].

The compressive strength and the elastic modulus derived from the stress versus strain curves are further presented in Fig. 11 (b). With the dosage of calcium hydroxide increasing from 0% to 6% in the mixture B, the compressive strength of the combined mixtures increased from 37.6 kPa to 93.8 kPa, and the elastic modulus of the combined mixtures increased from 461 kPa to 1355.3 kPa. As stated, more ettringite would form in the presence of calcium hydroxide, leading to faster strength gain and a more rigid structure. Typically, the compressive strength and elastic modulus reported for 3D printed concrete at the age of 5 min are lower than 10 kPa and 100 kPa, respectively [58]. In this study, both the compressive strength and the elastic modulus of the combined mixtures were several times higher than that of the typical 3D printed concrete, even for the one without the addition of calcium hydroxide (A-B0).

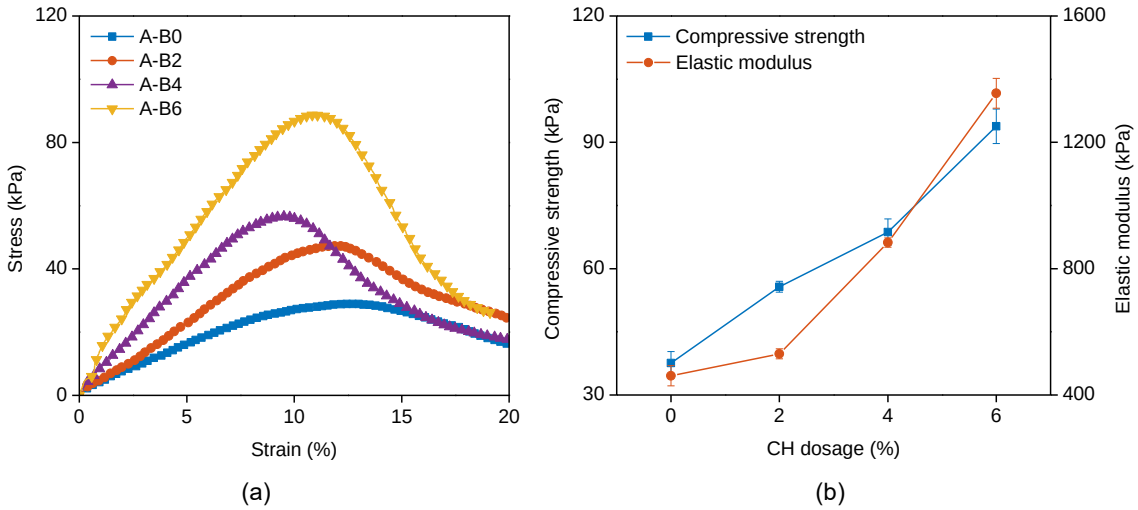

Fig. 11 (a) Stress-strain curves of combined mixtures and (b) compressive strength and elastic modulus of combined mixtures with different calcium hydroxide (CH) dosages at the age of 5 minutes (points in the graph represent mean values, n = 2).

In addition, the yield stress evolution of the combined mixtures was recorded by using the slow penetration test (see Fig. 12). It can be seen that all curves exhibited an almost exponential course. Due to the loading limitation of 3 kN, the maximum stress that can be measured amounted to around 5.7 MPa. For all combined mixtures, the yield stress reached the limitation within 30 min. In another study, the yield stress of 3D printable concrete was merely 1.1 kPa after more than 3 h, which was significantly lower than the yield stress of the combined mixtures tested in this study [37]. As such, it can be expected that a much higher critical height can be achieved by using the twin-pipe pumping technology over others. However, it should be noted that such a fast strength gain may also involves some potential problems such as shrinkage cracking and weak interface between layers [59, 60].

Another interesting point is that the yield stress of the mixture A-B2 was lower than that of the mixtures A-B4 and A-B6 in the first 15 minutes, and thereafter, overtook the yield stress of these two mixtures. This phenomenon was also observed in the P-wave velocity evolution where the value of the mixture A-B2 exceeded that of the mixtures A-B4 and A-B6 after around 15 minutes (see Fig. 9). This is also reflected by the shorter dormant period and the higher hydration peak value of the combined mixture A-B2 (see Fig. 10 (a)). As described above, incorporating more

calcium hydroxide in the reaction was beneficial for more precipitation of ettringite in the beginning, while the hydration rate can be reduced after a certain period due to the dilution effect.

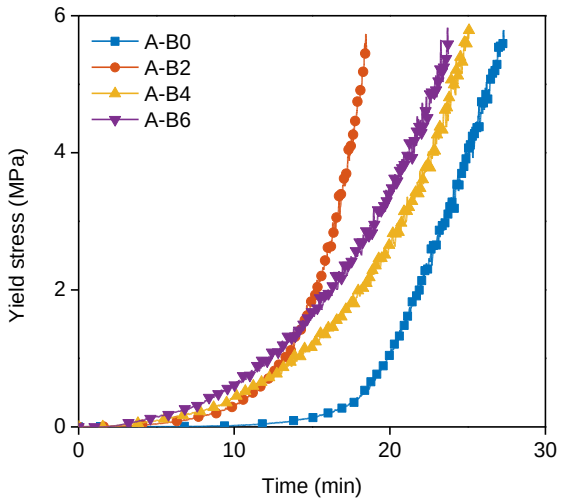

Fig. 12 Yield stress evolution measured in slow penetration tests.

3.3 Mechanical behavior at hardened stage

The flexural strength and compressive strength of the combined mixtures with different dosages of calcium hydroxide were measured at the age of 7 days by using mold cast specimens, as shown in Fig. 13. The mixture A-B6 with the highest dosage of calcium hydroxide presented the worst mechanical performance, where the lowest flexural strength of 6.4 MPa and the lowest compressive strength of 49.8 MPa were obtained. A one-way ANOVA test was further used to statistically analyze the flexural strength and compressive strength of the specimens. A p-value less than 0.05 ($p < 0.05$) was considered statistically significant. According to the results, no significant difference was observed when comparing the flexural strength of each series, while the compressive strength of the mixture A-B6 (6% calcium hydroxide) was significantly lower as compared to that of the mixtures A-B0 and A-B4. As mentioned above, this could be due to the dilution effect of adding calcium hydroxide to the matrix.

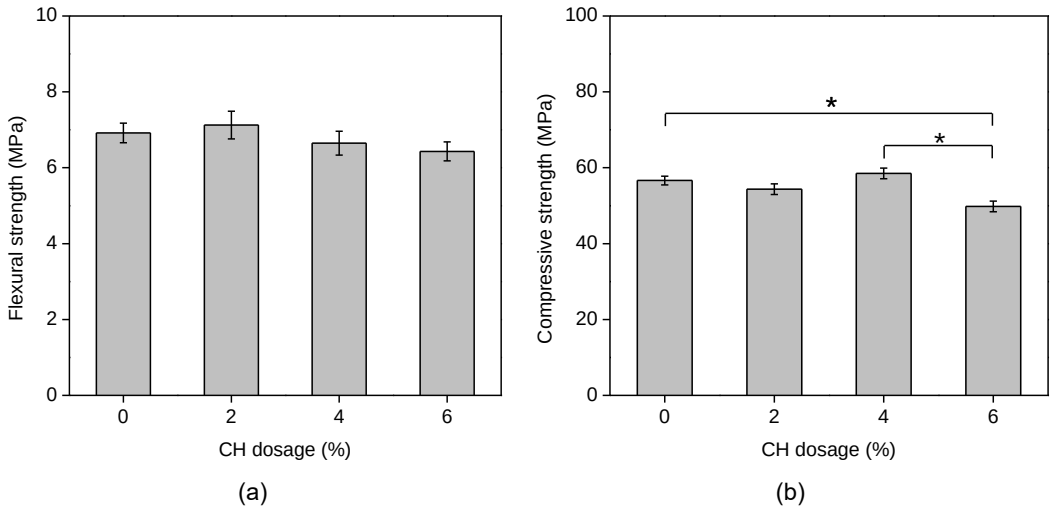

Fig. 13 Strength characteristics of combined mixtures (a) flexural strength and (b) compressive strength (error bars represent the standard error, n=3 for flexural strength, n=6 for compressive strength, the symbol * indicates a significant difference with a level of $p < 0.05$).

To further investigate the mechanical integrity of 3D printed specimens, the mixture A-B2 was selected. The flexural strength and compressive strength of the 3D printed specimens tested in three loading directions are shown in Fig. 14 (a) and (b), respectively. As compared to the flexural strength of mold cast specimens (7.1 MPa), the flexural strength measured in the loading direction F1 obtained a lower value (5.8 MPa). A strength reduction of 18% compared to the mold cast specimens was found. Such a strength reduction was due to the presence of the interlayer bond between filaments. With the fleet hydration rate after blending the constituent mixtures A and B, the surface moisture would lose as the consumption of water to yield ettringite and the evaporation with increased temperature [61, 62]. This would leave the surface to be drier and more rigid, resulting in limited bonds and a more porous interlayer region. As a result, the flexural strength F1 was lower, where the maximum bending stress was perpendicular to the weak interlayer [63]. Nevertheless, the flexural strength F1 of the mixture A-B2 was drastically higher than the one using limestone powder suspension as the second stream in previous studies, where the strength reduction was more than 50% compared to that of the mold cast specimens [22].

In the case of the loading directions F2 and F3, a higher strength was observed due to more densification occurring along the pumping and extrusion process [64]. In addition, a one-way ANOVA test was further used to statistically analyze the flexural strength and compressive strength

of the specimens. Similar, a p-value less than 0.05 ($p < 0.05$) was considered statistically significant. According to the results, no significant difference was observed when comparing the flexural strength of mold cast specimens with the 3D printed specimens loaded in direction F1. In addition, the compressive strength of each series showed no significant difference. Moreover, all specimens under different loading directions presented a typical conical failure even with the formation of striations (see Fig. 15). The results indicated the quite good mechanical performance of 3D printed specimens by using two reactive streams containing CSA and Portland cement.

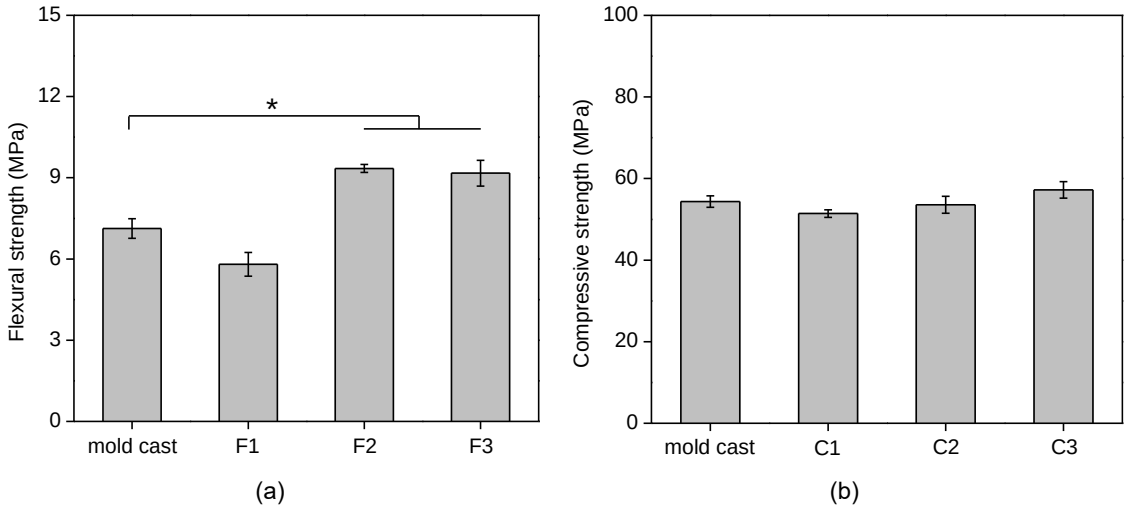

Fig. 14 Strength characteristics of 3D printed specimens (a) flexural strength and (b) compressive strength (error bars represent the standard error, n=3 for flexural strength, n=6 for compressive strength, the symbol * indicates a significant difference with a level of $p < 0.05$).

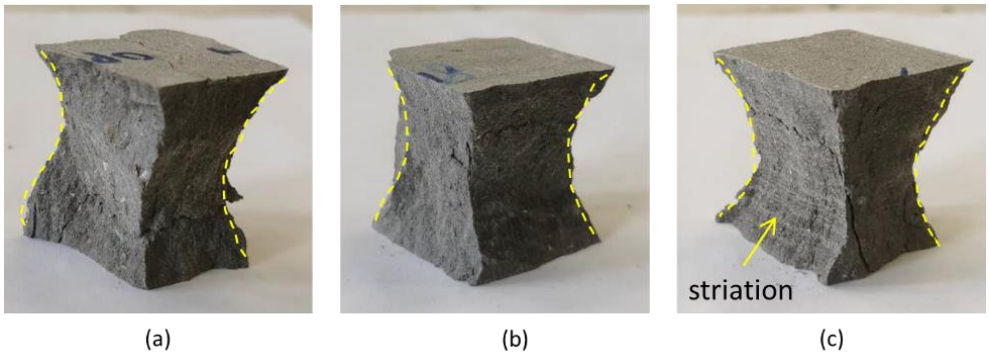

Fig. 15 Failure patterns of printed specimens in compression, (a) loading direction C1, (b) loading direction C2, and (c) loading direction C3.

4 Conclusions

In the present study, the development of a calcium sulfoaluminate (CSA)-Portland cement binary system for the twin-pipe pumping (TPP) technology is demonstrated. Based on the experimental results and discussion, the following conclusions can be drawn.

The alkali content in the Portland cement mixture alone was not sufficient for the fast stiffening required for the TPP process, while this problem can be overcome with the addition of small amounts of calcium hydroxide. Its addition resulted in destroying the retardation effect produced by ulexite and thereafter a fast solidification.

Abundant calcium hydroxide will reduce the hydration rate at later ages due to the dilution effect, as indicated by the P-wave velocity evolution and yield stress evolution. This is further reflected by the lower mechanical strength of the mold cast specimens with higher content of calcium hydroxide.

Nevertheless, because both constituent mixtures can stiffen independently, weakness that arises out of limestone-based striations is eliminated. By using 18 mixing baffles in the static mixer, no significant difference was observed when comparing the compressive strength of 3D printed specimens and mold cast specimens. Moreover, the flexural strength F2 and F3 was even higher than that of the mold cast specimens due to the compaction effect.

Acknowledgements

The authors acknowledge the financial support provided by Industrial Research Fund towards the StarTT Twinpipe project, and by SIM (Strategic Initiative Materials in Flanders) and VLAIO (Flanders agency for innovation & entrepreneurship) towards the 3D2BGreen project.

References

[1] G. Ma, R. Buswell, W.R. Leal da Silva, L. Wang, J. Xu, S.Z. Jones, Technology readiness: A global snapshot of 3D concrete printing and the frontiers for development, Cem. Concr. Res., 156 (2022) 106774, https://doi.org/10.1016/j.cemconres.2022.106774.

[2] G. De Schutter, K. Lesage, V. Mechtcherine, V.N. Nerella, G. Habert, I. Agusti-Juan, Vision of 3D printing with concrete — Technical, economic and environmental potentials, Cem. Concr. Res., 112 (2018) 25-36, https://doi.org/10.1016/j.cemconres.2018.06.001.

[3] S. Ramakrishnan, S. Kanagasuntharam, J. Sanjayan, In-line activation of cementitious materials for 3D concrete printing, Cem. Concr. Comps., 131 (2022) 104598, https://doi.org/10.1016/j.cemconcomp.2022.104598.

[4] D. Lowke, D. Talke, I. Dressler, D. Weger, C. Gehlen, C. Ostertag, R. Rael, Particle bed 3D printing by selective cement activation – Applications, material and process technology, Cem. Concr. Res., 134 (2020) 106077, https://doi.org/10.1016/j.cemconres.2020.106077.

[5] F.P. Bos, C. Menna, M. Pradena, E. Kreiger, W.R.L. da Silva, A.U. Rehman, D. Weger, R.J.M. Wolfs, Y. Zhang, L. Ferrara, V. Mechtcherine, The realities of additively manufactured concrete structures in practice, Cem. Concr. Res., 156 (2022) 106746, https://doi.org/10.1016/j.cemconres.2022.106746.

[6] F. Heidarnezhad, Q. Zhang, Shotcrete based 3D concrete printing: State of art, challenges, and opportunities, Constr. Build. Mater., 323 (2022) 126545, https://doi.org/10.1016/j.conbuildmat.2022.126545.

[7] S. Muthukrishnan, S. Ramakrishnan, J. Sanjayan, Technologies for improving buildability in 3D concrete printing, Cem. Concr. Comps., 122 (2021) 104144, https://doi.org/10.1016/j.cemconcomp.2021.104144.

[8] Y. Zhang, Y. Zhang, W. She, L. Yang, G. Liu, Y. Yang, Rheological and harden properties of the high-thixotropy 3D printing concrete, Constr. Build. Mater., 201 (2019) 278-285, https://doi.org/10.1016/j.conbuildmat.2018.12.061.

[9] Y. Qian, G. De Schutter, Enhancing thixotropy of fresh cement pastes with nanoclay in presence of polycarboxylate ether superplasticizer (PCE), Cem. Concr. Res., 111 (2018) 15-22, https://doi.org/10.1016/j.cemconres.2018.06.013.

[10] J. Kruger, S. Zeranka, G. van Zijl, An ab initio approach for thixotropy characterisation of (nanoparticle-infused) 3D printable concrete, Constr. Build. Mater., 224 (2019) 372-386, https://doi.org/10.1016/j.conbuildmat.2019.07.078.

[11] N. Roussel, Rheological requirements for printable concretes, Cem. Concr. Res., 112 (2018) 76-85, https://doi.org/10.1016/j.cemconres.2018.04.005.

[12] V. Vaitkevičius, E. Šerelis, V. Kerševičius, Effect of ultra-sonic activation on early hydration process in 3D concrete printing technology, Constr. Build. Mater., 169 (2018) 354-363, https://doi.org/10.1016/j.conbuildmat.2018.03.007.

[13] D. Jiao, K. Lesage, M.Y. Yardimci, K. El Cheikh, C. Shi, G. De Schutter, Quantitative assessment of the influence of external magnetic field on clustering of nano-Fe3O4 particles in cementitious paste, Cem. Concr. Res., 142 (2021) 106345, https://doi.org/10.1016/j.cemconres.2020.106345.

[14] S. Muthukrishnan, S. Ramakrishnan, J. Sanjayan, Effect of microwave heating on interlayer bonding and buildability of geopolymer 3D concrete printing, Constr. Build. Mater., 265 (2020) 120786, https://doi.org/10.1016/j.conbuildmat.2020.120786.

[15] Y. Tao, A.V. Rahul, K. Lesage, Y. Yuan, K. Van Tittelboom, G. De Schutter, Stiffening control of cement-based materials using accelerators in inline mixing processes: Possibilities and challenges, Cem. Concr. Comps., 119 (2021) 103972, https://doi.org/10.1016/j.cemconcomp.2021.103972.

[16] L. Reiter, T. Wangler, A. Anton, R.J. Flatt, Setting on demand for digital concrete – Principles, measurements, chemistry, validation, Cem. Concr. Res., 132 (2020) 106047, https://doi.org/10.1016/j.cemconres.2020.106047.

[17] D. Marchon, S. Kawashima, H. Bessaies-Bey, S. Mantellato, S. Ng, Hydration and rheology control of concrete for digital fabrication: Potential admixtures and cement chemistry, Cem. Concr. Res., 112 (2018) 96-110, https://doi.org/10.1016/j.cemconres.2018.05.014.

[18] W. Zhang, S. Li, J. Wei, Q. Zhang, R. Liu, X. Zhang, H. Yin, Grouting rock fractures with cement and sodium silicate grout, Carbonates and Evaporites, 33 (2018) 211-222, https://doi.org/10.1007/s13146-016-0332-3.

[19] P. Choi, J.H. Yeon, K.-K. Yun, Air-void structure, strength, and permeability of wet-mix shotcrete before and after shotcreting operation: The influences of silica fume and air-entraining agent, Cem. Concr. Comps., 70 (2016) 69-77, https://doi.org/10.1016/j.cemconcomp.2016.03.012.

[20] R.J. Flatt, T. Wangler, On sustainability and digital fabrication with concrete, Cem. Concr. Res., 158 (2022) 106837, https://doi.org/10.1016/j.cemconres.2022.106837.

[21] T. Wangler, R. Pileggi, S. Gürel, R.J. Flatt, A chemical process engineering look at digital concrete processes: critical step design, inline mixing, and scaleup, Cem. Concr. Res., 155 (2022) 106782, https://doi.org/10.1016/j.cemconres.2022.106782.

[22] Y. Tao, A.V. Rahul, K. Lesage, K. Van Tittelboom, Y. Yuan, G. De Schutter, Mechanical and microstructural properties of 3D printable concrete in the context of the twin-pipe pumping strategy, Cem. Concr. Comps., 125 (2022) 104324, https://doi.org/10.1016/j.cemconcomp.2021.104324.

[23] Y. Tao, A.V. Rahul, M.K. Mohan, K. Van Tittelboom, Y. Yuan, G. De Schutter, Blending performance of helical static mixer used for twin-pipe 3D concrete printing, Cem. Concr. Comps., 134 (2022) 104741, https://doi.org/10.1016/j.cemconcomp.2022.104741.

[24] J.P. Valdés, L. Kahouadji, O.K. Matar, Current advances in liquid–liquid mixing in static mixers: A review, Chem. Eng. Res. Des., 177 (2022) 694-731, https://doi.org/10.1016/j.cherd.2021.11.016.

[25] Y. Tao, A.V. Rahul, M.K. Mohan, G. De Schutter, K. Van Tittelboom, Recent progress and technical challenges in using calcium sulfoaluminate (CSA) cement, Cem. Concr. Comps., 137 (2023) 104908, https://doi.org/10.1016/j.cemconcomp.2022.104908.

[26] M.K. Mohan, A.V. Rahul, Y. Tao, G. De Schutter, K. Van Tittelboom, Hydration re-initiation of borated CSA systems with a two-stage mixing process: An application in extrusion-based concrete 3D printing, Cem. Concr. Res., 159 (2022) 106870, https://doi.org/10.1016/j.cemconres.2022.106870.

[27] A.V. Rahul, M. Santhanam, Evaluating the printability of concretes containing lightweight coarse aggregates, Cem. Concr. Comps., 109 (2020) 103570, https://doi.org/10.1016/j.cemconcomp.2020.103570.

[28] Y. Tao, A.V. Rahul, K. Lesage, K.V. Tittelboom, Y. Yuan, G.D. Schutter, Mechanical and microstructure properties of 3D printable concrete in the context of the twin-pipe pumping strategy, Cem. Concr. Comps., (2021), https://doi.org/10.1016/j.cemconcomp.2021.104324.

[29] R.P. Chhabra, J.F. Richardson, Non-Newtonian flow and applied rheology: engineering applications, Butterworth-Heinemann2011, https://www.sciencedirect.com/book/9780750685320/non-newtonian-flow-and-applied-rheology.

[30] M.K. Mohan, A.V. Rahul, K. Van Tittelboom, G. De Schutter, Rheological and pumping behaviour of 3D printable cementitious materials with varying aggregate content, Cem. Concr. Res., 139 (2021) 106258, https://doi.org/10.1016/j.cemconres.2020.106258.

[31] NBN EN 196-3:2005, Methods of testing cement - Part 3: Determination of setting times and soundness, 2005, https://www.nbn.be/shop/en/standard/nbn-en-196-3-2005_7181/.

[32] H.W. Reinhardt, C.U. Grosse, Continuous monitoring of setting and hardening of mortar and concrete, Constr. Build. Mater., 18 (2004) 145-154, https://doi.org/10.1016/j.conbuildmat.2003.10.002.

[33] J. Carette, S. Staquet, Monitoring the setting process of mortars by ultrasonic P and S-wave transmission velocity measurement, Constr. Build. Mater., 94 (2015) 196-208, https://doi.org/10.1016/j.conbuildmat.2015.06.054.

[34] N. Robeyst, E. Gruyaert, C.U. Grosse, N. De Belie, Monitoring the setting of concrete containing blast-furnace slag by measuring the ultrasonic p-wave velocity, Cem. Concr. Res., 38 (2008) 1169-1176, https://doi.org/10.1016/j.cemconres.2008.04.006.

[35] NBN EN 196-9, Methods of Testing Cement- Part 9: Heat of Hydration- Semi-adiabatic Method, British Standard, 2010, https://www.nbn.be/shop/en/standard/nbn-en-196-9-2010_17584/.

[36] R.J.M. Wolfs, F.P. Bos, T.A.M. Salet, Correlation between destructive compression tests and non-destructive ultrasonic measurements on early age 3D printed concrete, Constr. Build. Mater., 181 (2018) 447-454, https://doi.org/10.1016/j.conbuildmat.2018.06.060.

[37] U. Pott, D. Stephan, Penetration test as a fast method to determine yield stress and structural build-up for 3D printing of cementitious materials, Cem. Concr. Comps., 121 (2021) 104066, https://doi.org/10.1016/j.cemconcomp.2021.104066.

[38] D. Lootens, P. Jousset, L. Martinie, N. Roussel, R. Flatt, Yield stress during setting of cement pastes from penetration tests, Cem. Concr. Res., 39 (2009) 401-408, https://doi.org/10.1016/j.cemconres.2009.01.012.

[39] NEN EN 12390-5, Testing hardened concrete. Flexural strength of test specimens, 2019, https://www.nen.nl/nen-en-12390-5-2019-en-260971.

[40] NEN-EN 12390-3, Testing hardened concrete — Part 3: Compressive strength of test specimens, 2019, https://www.nen.nl/en/nen-en-12390-3-2019-en-260976.

[41] Q. Zhang, X. Shu, X. Yu, Y. Yang, Q. Ran, Toward the viscosity reducing of cement paste: Optimization of the molecular weight of polycarboxylate superplasticizers, Constr. Build. Mater., 242 (2020) 117984, https://doi.org/10.1016/j.conbuildmat.2019.117984.

[42] J. Liu, K. Wang, Q. Zhang, F. Han, J. Sha, J. Liu, Influence of superplasticizer dosage on the viscosity of cement paste with low water-binder ratio, Constr. Build. Mater., 149 (2017) 359-366, https://doi.org/10.1016/j.conbuildmat.2017.05.145.

[43] T. Huang, B. Li, Q. Yuan, Z. Shi, Y. Xie, C. Shi, Rheological behavior of Portland clinker-calcium sulphoaluminate clinker-anhydrite ternary blend, Cem. Concr. Comps., 104 (2019) 103403, https://doi.org/10.1016/j.cemconcomp.2019.103403.

[44] M.K. Mohan, A.V. Rahul, G. De Schutter, K. Van Tittelboom, Early age hydration, rheology and pumping characteristics of CSA cement-based 3D printable concrete, Constr. Build. Mater., 275 (2021) 122136, https://doi.org/10.1016/j.conbuildmat.2020.122136.

[45] R.J. Flatt, P. Bowen, Yield Stress of Multimodal Powder Suspensions: An Extension of the YODEL (Yield Stress mODEL), Journal of the American Ceramic Society, 90 (2007) 1038-1044, https://doi.org/10.1111/j.1551-2916.2007.01595.x.

[46] D. Jiao, C. Shi, Q. Yuan, X. An, Y. Liu, H. Li, Effect of constituents on rheological properties of fresh concrete-A review, Cem. Concr. Comps., 83 (2017) 146-159, https://doi.org/10.1016/j.cemconcomp.2017.07.016.

[47] G. Ma, Z. Li, L. Wang, Printable properties of cementitious material containing copper tailings for extrusion based 3D printing, Constr. Build. Mater., 162 (2018) 613-627, https://doi.org/10.1016/j.conbuildmat.2017.12.051.

[48] T.T. Le, S.A. Austin, S. Lim, R.A. Buswell, A.G. Gibb, T. Thorpe, Mix design and fresh properties for high-performance printing concrete, Mater. Struct., 45 (2012) 1221-1232, https://doi.org/10.1617/s11527-012-9828-z.

[49] J.-B. Champenois, M. Dhoury, C. Cau Dit Coumes, C. Mercier, B. Revel, P. Le Bescop, D. Damidot, Influence of sodium borate on the early age hydration of calcium sulfoaluminate cement, Cem. Concr. Res., 70 (2015) 83-93, https://doi.org/10.1016/j.cemconres.2014.12.010.

[50] W. Chen, X. Ling, Q. Li, B. Yuan, B. Li, H. Ma, Experimental evidence on formation of ulexite in sulfoaluminate cement paste mixed with high concentration borate solution and its retarding effects, Constr. Build. Mater., 215 (2019) 777-785, https://doi.org/10.1016/j.conbuildmat.2019.04.242.

[51] H. Chen, P. Feng, S. Ye, W. Sun, The coupling effect of calcium concentration and pH on early hydration of cement, Constr. Build. Mater., 185 (2018) 391-401, https://doi.org/10.1016/j.conbuildmat.2018.07.067.

[52] A. Kumar, G. Sant, C. Patapy, C. Gianocca, K.L. Scrivener, The influence of sodium and potassium hydroxide on alite hydration: Experiments and simulations, Cem. Concr. Res., 42 (2012) 1513-1523, https://doi.org/10.1016/j.cemconres.2012.07.003.

[53] N. De Belie, C. Grosse, J. Kurz, H.-W. Reinhardt, Ultrasound monitoring of the influence of different accelerating admixtures and cement types for shotcrete on setting and hardening behaviour, Cem. Concr. Res., 35 (2005) 2087-2094, https://doi.org/10.1016/j.cemconres.2005.03.011.

[54] M.A.G. Aranda, A.G. De la Torre, 18 - Sulfoaluminate cement, in: F. Pacheco-Torgal, S. Jalali, J. Labrincha, V.M. John (Eds.) Eco-Efficient Concrete, Woodhead Publishing2013, pp. 488-522, https://doi.org/10.1533/9780857098993.4.488.

[55] I.A. Chen, C.W. Hargis, M.C.G. Juenger, Understanding expansion in calcium sulfoaluminate–belite cements, Cem. Concr. Res., 42 (2012) 51-60, https://doi.org/10.1016/j.cemconres.2011.07.010.

[56] G.L. Valenti, M. Marroccoli, M.L. Pace, A. Telesca, Discussion of the paper "Understanding expansion in calcium sulfoaluminate–belite cements" by I.A. Chen et al., Cem. Concr. Res. 42 (2012) 51–60, Cem. Concr. Res., 42 (2012) 1555-1559, https://doi.org/10.1016/j.cemconres.2012.08.002.

[57] N.C. Consoli, M.A. Vendruscolo, A. Fonini, F.D. Rosa, Fiber reinforcement effects on sand considering a wide cementation range, Geotextiles and Geomembranes, 27 (2009) 196-203, https://doi.org/10.1016/j.geotexmem.2008.11.005.

[58] R.J.M. Wolfs, F.P. Bos, T.A.M. Salet, Early age mechanical behaviour of 3D printed concrete: Numerical modelling and experimental testing, Cem. Concr. Res., 106 (2018) 103-116, https://doi.org/10.1016/j.cemconres.2018.02.001.

[59] J.-L. Tao, C. Lin, Q.-L. Luo, W.-J. Long, S.-Y. Zheng, C.-Y. Hong, Leveraging internal curing effect of fly ash cenosphere for alleviating autogenous shrinkage in 3D printing, Constr. Build. Mater., 346 (2022) 128247, https://doi.org/10.1016/j.conbuildmat.2022.128247.

[60] Y. Weng, M. Li, D. Zhang, M.J. Tan, S. Qian, Investigation of interlayer adhesion of 3D printable cementitious material from the aspect of printing process, Cem. Concr. Res., 143 (2021) 106386, https://doi.org/10.1016/j.cemconres.2021.106386.

[61] J. Kruger, G. van Zijl, A compendious review on lack-of-fusion in digital concrete fabrication, Additive Manufacturing, 37 (2021) 101654, https://doi.org/10.1016/j.addma.2020.101654.

[62] R.J.M. Wolfs, F.P. Bos, T.A.M. Salet, Hardened properties of 3D printed concrete: The influence of process parameters on interlayer adhesion, Cem. Concr. Res., 119 (2019) 132-140, https://doi.org/10.1016/j.cemconres.2019.02.017.

[63] H. Liu, C. Liu, Y. Wu, G. Bai, C. He, R. Zhang, Y. Wang, Hardened properties of 3D printed concrete with recycled coarse aggregate, Cem. Concr. Res., 159 (2022) 106868, https://doi.org/10.1016/j.cemconres.2022.106868.

[64] A.V. Rahul, M. Santhanam, H. Meena, Z. Ghani, Mechanical characterization of 3D printable concrete, Constr. Build. Mater., 227 (2019) 116710, https://doi.org/10.1016/j.conbuildmat.2019.116710.